Research Article Vol. 30, No. 2 / 17 Jan 2022 / Optics Express 2173
Optics EXPRESS

Near-infrared, visible, and ultraviolet lidar echo emulator

MÓNICA RODRÍGUEZ-CORTINA,[1,2,*] PAWEL ADAMIEC,[1] JUAN BARBERO,[1] MANUEL CAÑO-GARCÍA,[2] XABIER QUINTANA,[2] AND MORTEN ANDREAS GEDAY[2]

[1]ALTER TECHNOLOGY TÜV NORD S.A.U., Calle Majada, 3, 28760 Tres Cantos (Madrid), Spain
[2]CEMDATIC, ETSI Telecomunicación. Universidad Politécnica Madrid. Avda. Complutense 30, 28040 Madrid, Spain
*monica.rodriguez@altertechnology.com

Abstract: A compact and cost effective NIR-VIS-UV lidar echo emulator (LEE) was designed and manufactured as a compact breadboard. The LEE is an application specific optical pulse shaper delivering a short lidar return (echo) in the ns range overlapped with a long lidar return in the µs range with a repetition rate from 100 Hz – 500 Hz. The short echo power levels are in the range from 0.2–200 nW, whereas the long echo powers from 0.1–25 pW. The coarse power tuning between the two kind of echoes is done using variable attenuators. LEE provides three operation modes: short echo, long echo, or both echoes overlapped. In the overlapping mode, the power difference between the echoes exceeds 60 dB.

1. Introduction

Lidar is an active remote sensing technique that has become an essential system for atmospheric and land surface remote sensing. In the last two decades, lidar systems have been part of numerous space missions such as CALIPSO (NASA, 2006) [1] or ADM Aeolus (ESA, 2018) [2], among others. Nowadays, one of the main challenges of the space missions is to implement a complex lidar instrument on a small satellite platform with limited resources. The limiting factors are the telescope size and detector size; therefore, the receiver and detector noise are both critical parameters. The detector and the following amplifier stages must be as noiseless as possible. HgCdTe (MCT) avalanche photodiode (APD) detectors are currently the promising candidates due to their exceptional performance in terms of high linear gain, low excess noise, high quantum efficiency and low dark current at low temperature [3–5]. However, even the MCT APD detector must be optimized to address the most challenging lidar applications like forthcoming MERLIN-ESA mission [6].

To fully characterize the optical parameters of the MCT APD detector modules, a device capable of emulating the return echoes of a real lidar system operating in space, where the short powerful echo (such as aerosol/cloud for example) is superposed on the long faint echo (atmospheric background), is necessary. One option is the optical pulse shaper (OPS). However, it needs to meet certain requirements according to pulse width of echoes (on the order of ns to µs) and large dynamic range (60 dB), which is required to correctly resolve the power and the shapes of the lidar echoes. Ultrafast OPS [7,8] obtain necessary dynamic range, but they provide pulses too short for this application. In the ns-scale, more techniques are available starting from the time varying electronic signals by means of arbitrary waveform generators (AWGs) or optical arbitrary waveform generators (OAWGs); however, their dynamic range is limited to 48 dB when using 16-bit analog-to-digital converters [9]. Other approach is the combination of optical modulators such as acousto-optic modulator (AOM) or electro-optical modulators (EOM) which can be used to obtain arbitrary pulse shaping in the necessary time, however the dynamic range could be obtained only if several stages are used. Another technique is to use two-stage amplifiers

#439960 https://doi.org/10.1364/OE.439960
Journal © 2022 Received 11 Aug 2021; revised 3 Dec 2021; accepted 3 Dec 2021; published 10 Jan 2022

Optics EXPRESS

[10,11], where a temporal deformation of ns pulses occurs during amplification processes when the amplifier is operated at saturation level. However, in these techniques little importance is given to the dynamic range of the pulses. Furthermore, these techniques only show a peak or two of equal size, and our goal is to obtain two waveforms of completely different shapes at the same time with a range of 60 dB between their maxima. The OPSs that most closely resemble what is needed, is the system developed by Wan [12] and our first lidar echo emulator (LEE) [13]. The first OPS [12] allows pulse shaping from 20 ns to 4 µs and micro-pulses with full width at half maximum (FWHM) of 20 ns can be obtained based on the longer 200 ns pulse with 17 dB dynamic range between two pulses. Our first LEE [13] also could produce both echoes, called long echo (LE) a base pulse – pedestal, and short echo (SE) in two separate channels (two set of drivers, lasers). Moreover, the difference between the echoes was 60 dB, controlled with variable attenuators. However, our initial approach only operates at 1064 nm and the system was bulky and expensive, because each echo was produced by separate systems. Recently, we have developed an OPS based on the emulation technique of multiple overlapped return echoes of a spatial lidar with 100 dB dynamic resolution by means of the optical delay line [14] which also fulfills the requirements for lidar echo discrimination.

Since MCT APD span infrared (IR), visible (VIS) and even ultraviolet (UV) spectral range, in this paper, we present a new design of the LEE suitable to characterize these detectors in the full set of wavelengths: UV, VIS, and NIR. Moreover, a substantial reduction in the number of components and size, hence costs, was achieved by applying the multiple overlapped technique to generate the two echoes at the same time. First, the challenges are explained in the section 2, followed by the brief explanation of the fundamental theory in the section 3. Next, the overall design together with each subsystem is described in depth in the section 4. The obtained results are presented in the section 5 and concluded in section 6.

2. Challenges and requirements

The features of the backscatter light (lidar return or echo) that the system must emulate to characterize the MCT APD are shown in the Fig. 1. There are two types of echoes: the short echo with pulse width < 10 ns and adjustable peak power between 0.2 to 200 nW, and the long echo with pulse width = 270 µs and adjustable peak power between 0.1 to 25 pW. The short echo emulates the pulse emitted by the laser after impacting particles suspended in a volume along the laser beam; and long echo emulates a background molecular scattering or semi-transparent clouds along the distance or altitude. The shape of LE is defined by the start power (P_{min}), the endpower (P_{max}), the duration of the ramp (t_{ramp}) and total duration of the LE (t_{total}), which will always in this implementation be 270 µs. The SE is much more powerful than the LE, therefore one of the challenges is to generate a power drop between pulses that can reach 60 dB (when the short pulse has the maximum level of peak power, and the LE has the minimum level).

These requirements arose because the detector (in our case MCT APD directly hybridized with a custom designed CMOS readout integrated circuit (ROIC)) must allow for detection of the return signals with a photon noise limited SNR over the full optical dynamic power range of space lidar signals, up to 60 dB, including signal fluxes below a single photon per observation time slot. Moreover, the temporal resolution should be also considered since the parasitic tails can bias the measurements in the case of differential absorption lidar (DIAL) [15]. Therefore, there is a need for a perfect source to observe detection chain impact.

To characterize the detector in the required wavelength range the LEE must emulate the return echoes at 1064 nm, 532 nm and 355 nm which are the reference wavelengths of lidar systems in space missions.

Optics EXPRESS

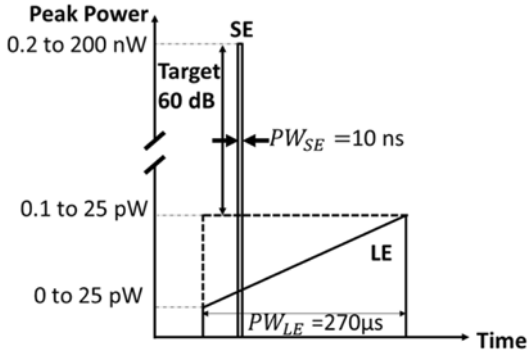

Fig. 1. Requirements for short (SE) and long echo (LE). Pulse width of the short echo. (PW_{SE}) and pulse width of the long echo (PW_{LE}).

3. Materials and methods

3.1. Non-linear materials

Since no semiconductor lasers are available at the wavelengths of 532 nm and 355 nm in the photonic market, second order nonlinear processes are used in our design, such as second harmonic generation (SHG) for 532 nm and sum frequency generation (SFG) for 355 nm. Here we only give a very brief explanation of these processes and we encourage the readers to consult original literature such as [16].

SHG or frequency doubling is a common application that utilizes the properties of a nonlinear crystal, where two input photons with the same wavelength λ_1 are combined through a nonlinear process to generate a third photon at $\lambda_1/2$ a relationship conveniently expressed in angular frequencies of the light [Eq. (1)], independently of the media of the light.

$$\omega_2 = 2\omega_1 \ \propto \frac{1}{\lambda_1} + \frac{1}{\lambda_1} \tag{1}$$

Nonlinear crystals such as KH2PO4 (KDP), LiNbO3 (LN), KTiOPO4 (KTP), β-BaB2O4 (β-BBO), LiB3O5 (LBO) and KBe2BO3F (KBBF) are widely used to implemented SHG technique in the visible range [17,18]. However, the most frequent configuration for SHG is by using KTP crystal, due to its high nonlinear conversion coefficient, wide acceptance angle, high allowed temperature, small walk-off angle and relativity high damage threshold [19]. Other notable advantage is that the phase matching in the KTP crystal is obtained at room temperature (23°C) because the birefringence is only marginally temperature dependent. In our case, phase matching is accomplished by angle tuning method, which involves precise angular orientation of the crystal with respect to the propagation direction of the incident light and proper selection of the polarizations of the interacting beams.

Finally, KTP is relatively low cost component compared to other valid non-linear crystals for this purpose, hence it is widely used in solid state lasers (for example, neodymium-YAG laser) [20].

The wave vectors, $k(\omega)$ and $k(2\omega)$, may be defined as

$$k(\omega) = \omega \cdot \frac{n(\omega)}{c} \tag{2}$$

$$k(2\omega) = 2\omega \cdot \frac{n(2\omega)}{c} \tag{3}$$

with $n(\omega)$ being the refractive index at 1064 nm, being the refractive index at 532 nm, and c being the speed of light. The phase matching condition requires $n(\omega) = n(2\omega)$, which is normally not

Optics EXPRESS

achieved due to dispersion. However, birefringent materials have different refractive indices for different polarizations, in uniaxial systems: ordinary (o) and extraordinary (e) refractive indices, the latter of which depends on the incidence angle. Therefore, the phase matching condition may be obtained for these two refractive indices: $n_e(\omega) = n_o(2\omega)$ at given angles. KTP is actually a biaxial optical crystal and thus we are using type II phase matching [21]. Figure 2 shows the two polarized components of the incident fundamental wave (FW) electric field (E_{e^ω} and E_{o^ω}) behaving as ordinary (non-deviated) and extraordinary (deviated) waves with the frequency ω at the input face of KTP crystal. In the exit face of the crystal the phase matched beam at frequency 2ω has been deviated due to the birefringence of the KTP. Also, the propagation directions of the FW at wavelength of $\lambda_1 = 1064$ nm and SHG ($E_{e^{2\omega}}$) at $\lambda_2 = 532$ nm are shown [19]. This figure also shows the walk-off angles $\rho_1 = 0$ mrad, $\rho_2 = 3.15$ mrad and $\rho_3 = 4.12$ mrad.

Maximizing conversion efficiency is often the main objective [22–24] but, in our application, it is not that important factor because the optical powers of the echoes at the LEE output should be very low (peak power range from pW to nW).

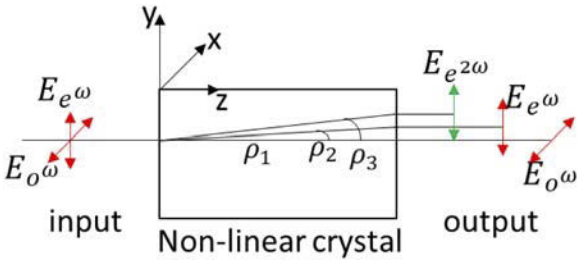

Fig. 2. Scheme of type-II phase matching for KTP crystals [19].

The sum frequency generation (SFG) technique is used to obtain at 355 nm beam. The SFG combines two input photons at λ_1 and λ_2 to generate an output photon at λ_3 [Eq. (4)]. 355 nm wavelength is obtained by sum of 1064 nm and 532 nm wavelengths.

$$\frac{1}{\lambda_3} = \frac{1}{\lambda_1} + \frac{1}{\lambda_2} \tag{4}$$

Since, in our case, the power at the output of the KTP crystal was not enough to generate the UV beam even with maximizing the efficiency, two periodically poled lithium niobate (PPLN) crystals are used. The PPLN is also a highly efficient medium for nonlinear wavelength conversion processes, but it is an engineered quasi-phase-matched crystal, which means that the orientation of the lithium niobate crystal is periodically inverted or periodically poled (PP). Moreover, the matching angle is fixed at 90 deg (normal incidence) and only temperature variation of the crystal is necessary, because the birefringence is strongly temperature dependent. Therefore, temperature matching is used in the two PPLNs for SFG in our LEE.

3.2. *Technique with two overlapping echoes*

The emulation technique of multiple overlapping echoes [14] was applied to superimpose short and long echo in the LEE. In brief, a waveform is generated with the two contiguous echoes (see Fig. 3(a)) by means of an optical pulse generator (OPG). This waveform pattern is introduced to the input IN of the setup shown in Fig. 4. The 50:50 optical coupler SX conducts the signal to two channels, a high-power channel (HPC) and low power channel (LPC). The delay line (optical fiber reel) is placed in the LPC. Therefore, the waveform pattern introduced in LPC suffers a delay compared to the pattern in the HPC. Finally, another optical coupler SY with 50:50 ratio joins the two channels, and the two overlapping echoes are obtained at the output OUT (see

Optics EXPRESS

Fig. 4). The obtained waveform at the output is shown in Fig. 3 (b). Variable attenuators (VA) are used in both channels to obtain the desired power level between both echoes.

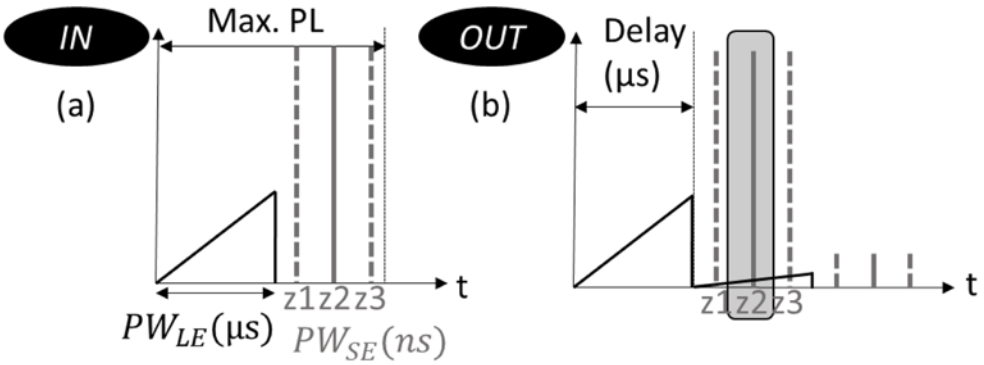

Fig. 3. Configuration of the input single waveforms (a) and output overlapped waveforms (b). Maximum pattern length (Max. PL).

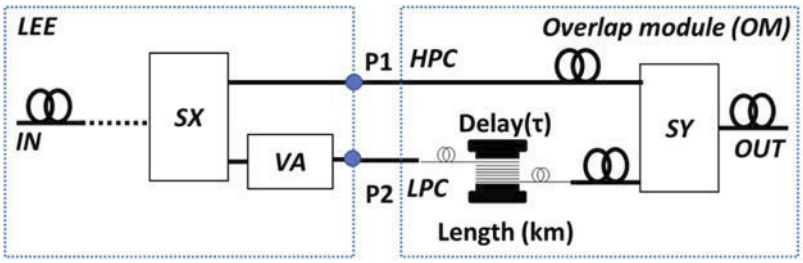

Fig. 4. Set-up for the technique of short and long echo overlapping.

It is worth to note that the short echo can be overlapped in any position within the long echo and as example three positions z1, z2, and z3 are depicted in the Fig. 3. Both the variable attenuators and the optical couplers are modified according to the operating wavelength (1064 nm or 532 nm) of the LEE, but not during the testing.

3.3. Measurements of echoes

Characterization of the described echoes requires the detectors which can resolve at least 60 dB of the dynamic range only for the power discrimination between the echoes. Considering the full dynamic resolution of the LEE as 100 dB, where the dynamic resolution is defined as the granularity of the power adjustment with respect to the maximum power [14], no commercial detector is available for this type of measurements. Therefore, three different photodetectors are used to characterize LEE: (i) Silicon Photodiode Thorlabs FDS02 (SIL) with the nominal responsivity of 0.01542 A/W at 1064 nm and 0.1851 A/W at 532 nm; (ii) UV-Enhanced Silicon avalanche photodiode Thorlabs APD410A2 (APD) with responsivity of 0.064 A/W at 1064 nm, 23.5 A/W at 532 nm and 8.5 W/A at 355 nm; and (iii) InGaAs photodiode Thorlabs FGA01FC (IGA) with nominal responsivity of 0.6874 A/W at 1064 nm. Both, SIL and IGA are in a reverse biased circuit with a 50 Ω load resistance. The transimpedance gain of APD is used with 250 kV/A (at 50 Ω). The three photodiodes were mutually calibrated using a 1-mW CW laser diode emitting at 1064 nm (Lumics LU1064M100) and a Rhode & Schwarz RTO1024 oscilloscope. For 532 nm only SIL and APD were mutually calibrated with a green laser pointer. For the

Optics EXPRESS

average power calibration, the Newport 2835-C-CAL and sensor head Newport 818-UV was employed.

4. LEE design

4.1. Overall system design

The NIR-VIS-UV LEE emulates the echoes at three wavelengths: 1064 nm, 532 nm, and 355 nm. Therefore, it consists of 3 internal modules NIR, VIS, and UV as shown in the Fig. 5. The NIR and VIS modules were designed and developed to generate single echo: short (mode 1) and long (mode 2) already presented in [25], or overlapped echoes (mode 3). In the case of the UV subsystem only one echo at a time can be generated due to the lack of optical components with low losses at this wavelength on the photonic market. The NIR and VIS wavelength are generated simultaneously, while the UV generation requires switching between NIR/VIS and UV inputs.

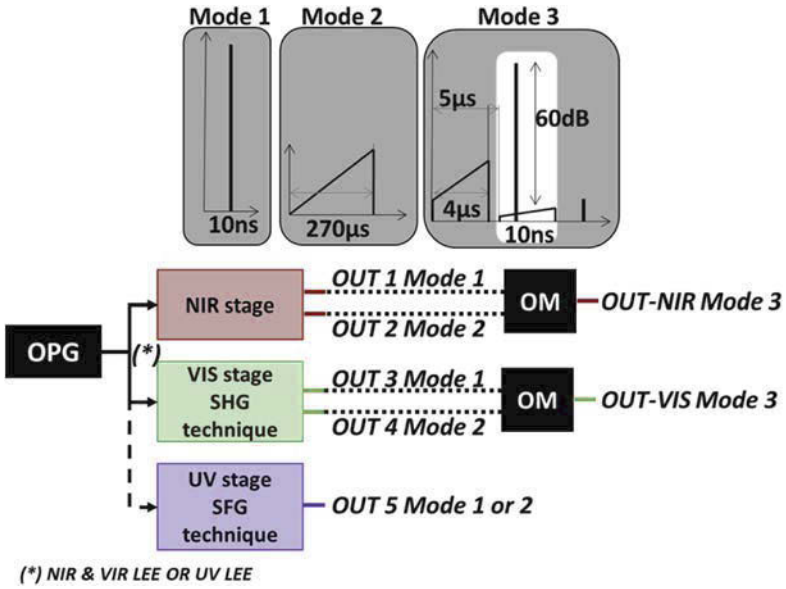

Fig. 5. Scheme of overall system design.

The overlapping of echoes is performed by means of the setup described in the section 3.2, however this set-up is not integrated inside the NIR-VIS-UV LEE, but it is an external overlapping module (OM) deployed outside of the equipment for easy exchange of the delay line to adjust necessary delays. Commercially available optical fibers suffer strong absorption in the wavelengths range shorter than telecom wavelengths: 1.5 dB/km at 1064 nm and ~ 20 dB/km at 532 nm [26], which make impossible to achieve 270 µs delays with necessary power requirements. At 355 nm the absorption can reach 100 dB [27]. However, considering that only discrimination with 60 dB between echoes is necessary, any delay line length can be used if the delay is longer than the remanence of the MCT APD under test i.e., 1 µs reported by Rothman et al. [5]. Therefore, in this application an optical fiber of 1 km was used resulting in 5 µs delay.

The modular design allows for great flexibility during the testing and further improvements in the future when the optical fibers will have less absorption at shorter wavelengths.

Only one laser at the wavelength of 1064 nm is used for entire system. The nonlinear wavelength conversion processes described in section 3.1 are used to obtain 532 nm and 355 nm emission. The chosen pigtailed semiconductor laser diode is LD-1064-PM-p1200, Innolume. The center wavelength is 1064.37 with FWHM = 3.26 nm (conditions: 1% duty cycle with 10 ns

Optics EXPRESS

pulse width) and the peak output power is 1.2 W. The threshold current was determined to be 61 mA at CW operation. The optical fiber is a polarization maintaining (PM) PANDA PM980 (the output light is polarized along the slow axis of PM fiber). The details about the waveform generation are given in the next section.

The short pulse is the most limiting factor, so an OPG with a minimum clock of 0.1 GHz is necessary. For this purpose, the OPM-LD-ps module is acquired from the manufacturer Optical Pulse Machines to generate both, the short and long pulse. This module is a "sandwich" of two boards: AWG and a thermo controlled electrical-to-optical (E/O) converter board (model OPM-LD-Lin). The AWG's clock rate is 1.8 GHz which enables generation of waveforms in resolution of sub-nanoseconds.

Software was developed in LabVIEW that allows reconfiguration of the relevant parameters of the pulse train: the shape of the waveform, duty cycle, bias level, trigger source, laser temperature, control low-pass filter settings, while monitoring of the laser diode working parameters.

4.2. Waveform design (configuration)

The maximum number of pulses (maximum Pulse Length (PL)) of OPG is 55200. As the AWG's clock rate is 1.8 GHz, each sample corresponds to 0.5556 ns. Therefore, the short echo is generated with 18 samples to get the pulse of 10 ns. In the case of the long echo, the generation of the pulse depends on the operation mode. For the mode 2, long pulse has a length of 270 µs, whereas in mode 3, with used delay of 5 µs the pulse length is 4 µs. From the maximum number of the samples and clock rate, the maximum PL which could be generated reads 30.669 µs corresponding to delay line of about 6 km without losing temporal resolution. However, OPG comes with six digital multipliers (x1, x2, x4, x8, x16 and x32) so the 270 µs pulse can be generated using the x16 multiplier with the temporal resolution of 9 ns. The long pulse is generated with repetition rate in the 100-500 Hz range.

4.3. System description

4.3.1. NIR stage

The scheme of the NIR module is shown in the Fig. 6, consider only the dotted part. The optical power from the OPG is split in two paths through a PM fiber coupler ***S1*** (PN1064R1A1, Thorlabs). The path with 99% of the optical power is used to generate the SHG and goes to VIS module. The second path with the rest of the optical power (1%) is used to generate the short or long echo in the NIR module described below.

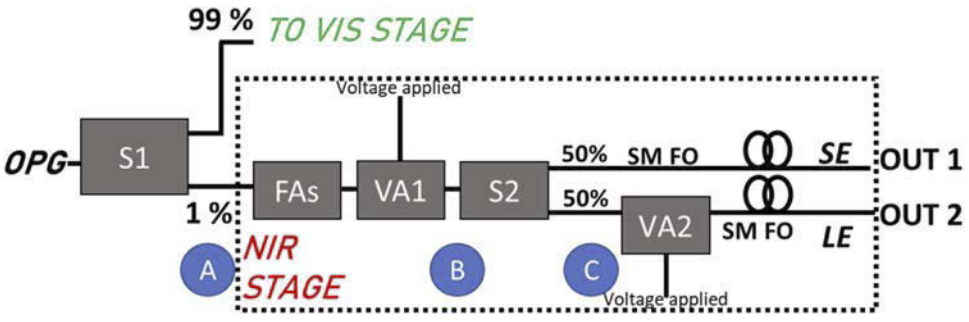

Fig. 6. Block diagram of the NIR stage – dotted rectangle.

First components in the optical path in the NIR module are three fixed attenuators (FA25T, Thorlabs, FAs). Each FA25T introduces an attenuation of 13 dB (@1064nm). Therefore, the total attenuation is 39 dB. Subsequently, a voltage-controlled optical attenuator ***VA1*** (V1000A,

Optics EXPRESS

Thorlabs) is used to adjust the desired peak power in two echoes. The maximum attenuation of this type of VA is < 45 dB.

An optical 50:50 splitter ***S2*** (TN1064R5A1B, Thorlabs) is used to separate the paths emulating the short and the long echoes. Additional variable attenuator ***VA2*** is set in the optical path to ***OUT 2***, and it is used to adjust the peak power of the long echo. A maximum level of 200 nW (-37 dBm) and a minimum level of 0.2 nW (-67 dBm) are required for the short echo, and a maximum level of 25 pW (-76 dBm) and a minimum level 0.1 pW (-100 dBm) for the long echo. The peak power at the output in each arm is set with the variable attenuators at maximum level for each echo. In the case of the SE channel, one variable attenuator ***VA1*** was necessary, whereas two variable attenuators ***VA1*** and ***VA2*** were used in the LE channel.

The three modes in the NIR module are obtained as following. In the mode 1, a SE with a peak power of 200 nW is obtained at ***OUT 1*** with ***VA1*** switched on (2.2V). Then, SE peak power can be decreased to 0.2 nW by applying a voltage from 2.2 V to 3.8 V on the ***VA1***. Similar procedure is used in the mode 2 where a LE with a peak power of 25 pW is obtained at ***OUT 2*** with ***VA1*** switched on (4.1V). However, only a voltage of 3.4 V on ***VA2*** is necessary to decrease the peak power to 0.1 pW for LE.

In the mode 3, the overlapping two echoes technique (see section 3.2) is applied. The delay line (optical fiber reel) is introduced outside the LEE through ***OUT 2*** connected to ***P2*** and coupler ***SY***, whereas ***OUT 1*** is connected directly to coupler ***SY***. The splitter ***SX*** from Fig. 3 refers to ***S2*** from Fig. 6 and the variable attenuators are readjusted to meet the power requirements of both echoes. The overlapping two echoes at 1064 nm is obtained at ***OUT NIR***.

4.3.2. VIS stage

The 99% of the optical power after ***S1*** enters the VIS module and is used to generate the 532 nm light as described in section 3.1. The scheme is shown in the Fig. 7. The SHG is reached by means of a KTP crystal (KTP-402, Eksma Optics) with dimensions 3 mm x 3 mm x 10 mm (Width x Height x Length). A crystal of this length leads to the beams displacement as follows: 1064 nm (e) = 31. 5 µm, 1064 nm (o) remains unchanged, and 532 nm (e) = 41.2 µm.

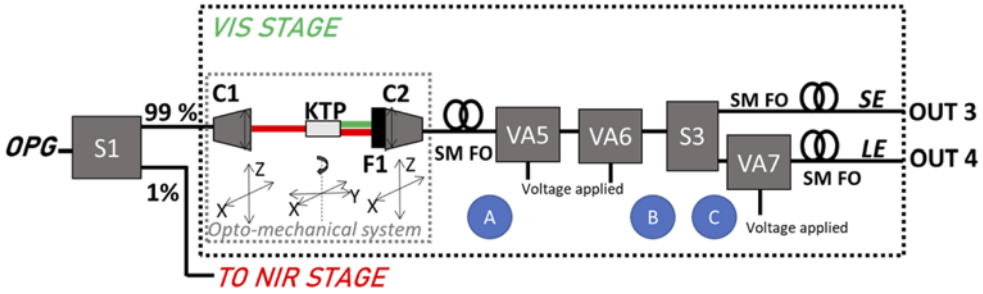

Fig. 7. Block diagram of VIS stage.

A collimator ***C1*** (PAF-X-2-C, Thorlabs) is used to match the beam to the KTP crystal cross-section The collimated beam is measured at the input facet of the crystal by means of a CMOS camera and the dimensions of the spot are 0.454 mm for X axis and 0.440 mm for Y axis.

The residual pump is removed using a short pass filter ***F1*** (FESH0550, Thorlabs) and the beam is focused again into the single mode fiber using an aspheric collimator C2 (CFS2-532-FC, Thorlabs). The collimator is located 45 mm from the KTP crystal (see the Fig. 8).

The peak power adjustment follows the same procedure as in the NIR module. Two variable attenuator ***VA5*** and ***VA6*** (V450F, Thorlabs) –analogue to ***VA1*** from NIR module– are used to adjust the desired power to the maximum level of the two echoes. The maximum attenuation of

Optics EXPRESS

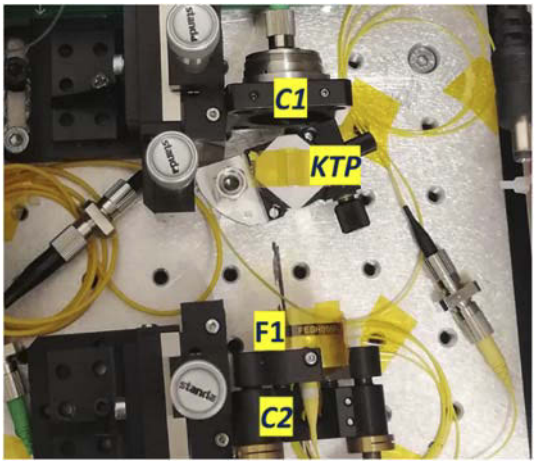

Fig. 8. The SHG setup in the VIS module.

this type is < 40 dB. The optical 50:50 coupler ***S3*** (TN532R5A1, Thorlabs) corresponds to ***S2*** in NIR module. Since the generated 532 nm beam has 1.23 µW. The maximum and minimum peak power in SE channel is adjusted with ***VA5*** and ***VA6*** and in LE channel, an additional variable attenuator ***VA7*** is necessary to achieve the required peak power level.

Like the NIR stage the VIS stage provides 3 working modes. In the mode 1, the SE with adjustable peak power is obtained at output ***OUT 3***. In the mode 2, the LE obtained at output ***OUT 4*** has also the power in the necessary range. In the mode 3, the overlapping two echoes technique (see section 3.2) is applied. Note that the attenuation of a conventional optical fiber, used as delay line, at 532 nm wavelength is around 18 dB/km, hence one order of magnitude higher as for 1064 nm. Therefore, the attenuation necessary to achieve the 60 dB drop between both echoes by the VIS variable attenuator is lower in comparison to the NIR.

4.3.3. UV stage

In the UV stage, the module SC19348-01-01 from HC Photonics is used to achieve the 355 nm beam at the output by introducing the 1064 nm beam directly from the OPG. The module consists of two PPLN crystals and a UV bandpass filter to remove unwanted wavelengths Fig. 9. As above mentioned, the temperature tuning is used for the phase matching, therefore crystals are buried in the thermoelectrically controlled ovens (TEC). The first 25 mm crystal is used to generate the 532 nm beam. The optimum operating temperature was found to be 32.9°C (see Fig. 10) using a Si detector. The second 10 mm crystal combines 1064 nm and 532 nm through SFG processes resulting in UV light at 355 nm. Here, the optimized temperature is found to be 26.4°C using an UV Enhanced Silicon Photodetector (818-UV/DB, Newport). Next, a UV bandpass filter ***F2*** (UG-11, Edmund Optics) is used to remove the pump beams. Finally, the UV beam is introduced into a multimode fiber with 200 µm core diameter and 0.22 numerical aperture (M91L01, Thorlabs).

4.3.4. Compact bread board

The three modules were mounted inside a transport unit as an elegant breadboard. All the necessary software was developed in the LabView environment to automatize maximally the operation of the NIR-VIS-UV LEE. The pictures of the unit are shown in the Fig. 11.

Optics EXPRESS

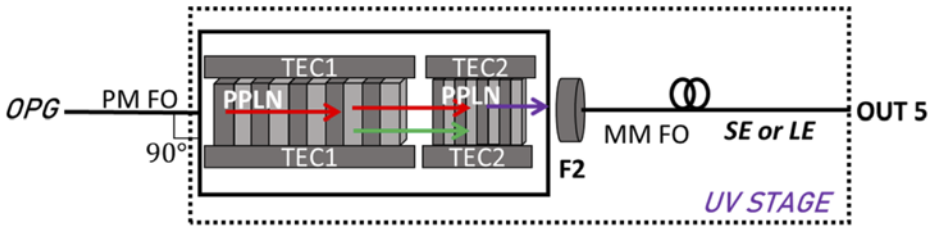

Fig. 9. Block diagram of UV stage.

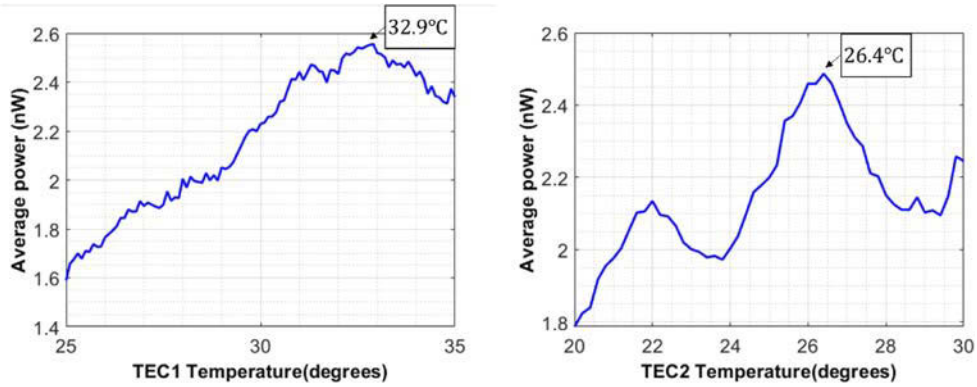

Fig. 10. The temperature evolution of the first crystal (left) and the second crystal (right) to achieve maximum optical output power.

Fig. 11. The realization of the LEE: hardware and software (left) and the top level inside NIR-VIS-UV LEE (right).

5. Results and discussion

The wavelength and FWHM of each beam are measured with the spectrometer (CCS200, Thorlabs) and are collected in the Table 1.

Table 1. Wavelenghts of the NIR-VIS-UV LEE.

	Wavelength	*FWHM*
NIR	1064.37 nm	3.26 nm
VIS	532.15 nm	1.13 nm
UV	355.12 nm	0.85 nm

Optics EXPRESS

Since the NIR-VIS-UV LEE operates in different modes, it is important that the initial shapes of the waveforms created by means of the OPG are maintained throughout the entire system changing only the power level due to necessary power scaling. Therefore, the evolution the short echo (mode 1) and long echo (mode 2) at different points (A, B, and C from Fig. 6) are shown in the Fig. 12 for NIR module. Both echoes are measured by means of IGA. The attenuation and a small delay that the signal suffers are due to the different optical fiber components in both paths. After this point, the NIR variable attenuators are used to obtain the maximum target values of peak power. For the SE the P_{peak} = 200 nW is reached with 33 dB attenuation, whereas for LE the P_{peak} = 0.2 nW requires 76 dB attenuation.

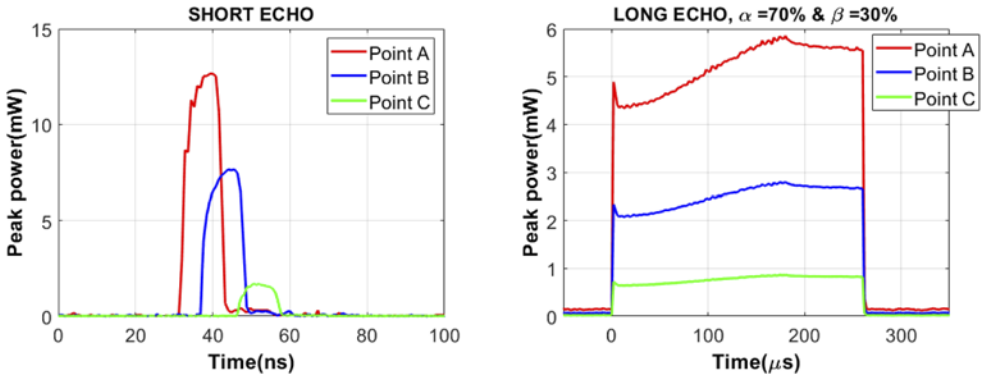

Fig. 12. Short and long echo at points A, B, and C of the NIR stage.

The overlapping of the two echoes (mode 3) is shown in Fig. 13. The signal in the low power channel is measured with an APD and the high-power channel with SIL and shown in the Fig. 13 (left) after power calibration according to section 3.3. The power difference between maxima of both echoes of 60 dB was obtained. The inset in the Fig. 13 (left) shows the shape of the short pulse in the logarithmic scale. However, due to oscilloscope limitations, the measurements only up to 30 dB can be taken, and within this range the parasitic tail can be estimated to be 6 ns.

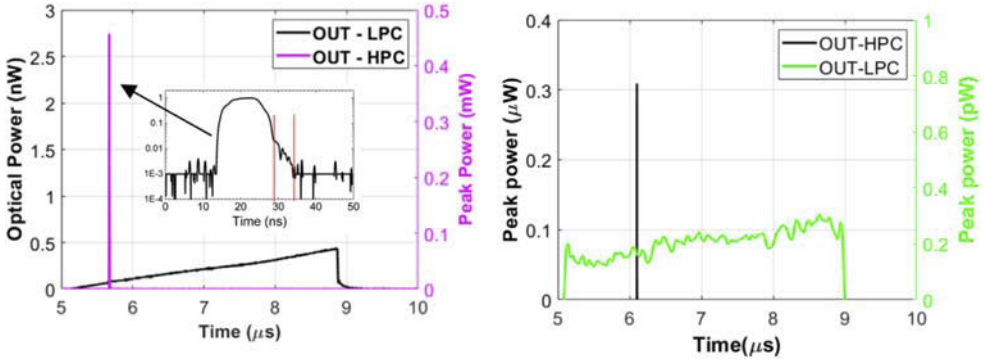

Fig. 13. Overlapping of the two echoes (mode 3) in the NIR stage and the inset that shows the normalized shape of the short pulse in the logarithmic scale (left) and in the VIS stage (right).

Similar measurements were taken at 532 nm in the VIS module. This time only APD was used due to its responsivity in the VIS range. However, the APD bandwidth of 10 MHz, leads to an artificial broadening of the short echo (mode 1). It can be seen at the left side in the Fig. 14

Optics EXPRESS

where the pump pulses with 10 ns and 20 ns are shown together with broadened SHG pulses. The measurement of the long echo (mode 2) is not affected by the detector bandwidth and the example of the ramp waveform is shown in the Fig. 14 at the right hand side.

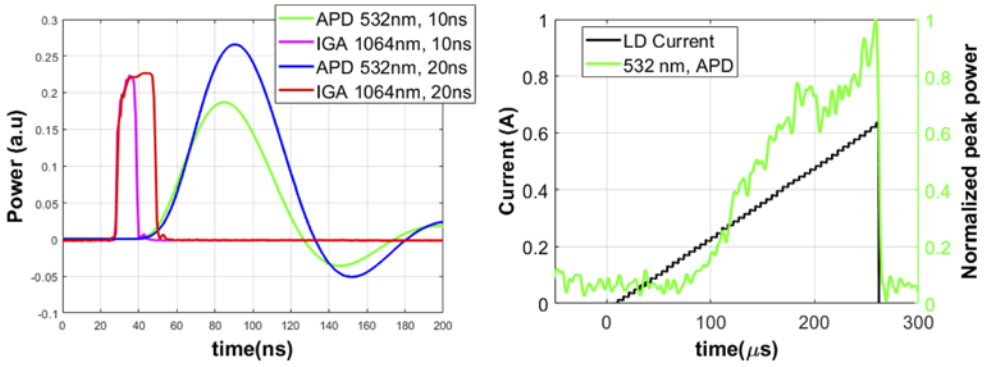

Fig. 14. The short echo (left) and ramp echo (right) measured by APD detector in VIS stage.

In the Fig. 13 (right), the measurement of the overlapping echoes (mode 3) in the VIS module is shown. The difference between the maxima of both echoes is 60 dB. In the case of the UV echoes, we only could measure the average power, due to the sensor bandwidth, and we found that both echoes reached necessary peak power levels using square pulses and considering the duty cycle. The acquisition of the waveforms was not possible with the available detectors.

6. Summary and conclusions

The NIR-VIS-UV LEE was designed and developed as modular compact breadboard. It allows emulation of lidar echoes with 60 dB discrimination between short and long echoes at a time in the NIR and VIS range using multiple echoes overlapping technique. Moreover, all modules provide short and long echo separately. Therefore, LEE could be used for characterization of the new MCT APD detectors with high dynamic range. The developed setup, as presented previously [14] provides a dynamic range of 60 dB, without any temporal tailing, although the characterization of the same is limited by the dynamic range of the employed, commercially available photodetectors.

Modular design allows for future improvements when new high performance optical components will become available in the shorter wavelengths. It allows also setting another power levels for different applications by choosing different attenuation levels.

Funding. Comunidad de Madrid (IND2017/TIC-7758, S2018/NMT-4326); Comunidad de Madrid, under the Multiannual Agreement with UPM in the line Support for R&D projects for Beatriz Galindo researchers, in the context of the V PRICIT; Gobierno de España (BG20/00136); Horizon 2020 Framework Programme (776390); Ministerio de Ciencia, Innovación y Universidades (PID2020-114172RB-C22).

Disclosures. The authors declare that there are no conflicts of interest related to this article.

Data availability. Data underlying the results presented in this paper are not publicly available at this time but may be obtained from the authors upon reasonable request.

References

1. D. M. Winker, J. R. Pelon, and M. P. McCormick, "CALIPSO mission: spaceborne lidar for observation of aerosols and clouds," Proc. SPIE Int. Soc. Opt. Eng. **4893**, 1–11 (2003).
2. A. G. Straume, A. Elfving, D. Wenham, F. de Bruin, T. Kanitz, D. Schuettemeyer, J. von Bismarck, F. Buscaglione, O. Lecrenier, and P. McGoldrick, "ESA's spaceborne lidar mission ADM-Aeolus: project status and preparations for launch," EPJ Web Conf. **176**, 04007 (2018).

Optics EXPRESS

3. I. Baker, C. D. Maxey, L. G. Hipwood, and K. Barnes, "Leonardo (formerly Selex ES) infrared sensors for astronomy: present and future," Proc. SPIE **9915**, 991505 (2016).
4. X. Sun, J. B. Abshire, J. D. Beck, P. Mitra, K. Reiff, and G. Yang, "HgCdTe avalanche photodiode detectors for airborne and spaceborne lidar at infrared wavelengths," Opt. Express **25**(14), 16589 (2017).
5. J. Rothman, P. Bleuet, J. Abergel, S. Gout, G. Lasfargues, L. Mathieu, J. Nicolas, J. Rostaing, S. Huet, P. Castelein, K. Aubaret, and O. Saint-Pé, "HgCdTe APDs detector developments at CEA/Leti for atmospheric lidar and free space optical communications," Proc. SPIE **11180**, 135 (2019).
6. A. Amediek, G. Ehret, A. Fix, M. Wirth, C. Büdenbender, M. Quatrevalet, C. Kiemle, and C. Gerbig, "CHARM-F—a new airborne integrated-path differential-absorption lidar for carbon dioxide and methane observations: measurement performance and quantification of strong point source emissions," Appl. Opt. **56**(18), 5182–5197 (2017).
7. A.S. Karar, R. Ghandour, I. Mahariq, S.A. Alboon, I. Maaz, B. Neji, and J.M.H. Barakat, "A Programmable Mode-Locked Fiber Laser Using Phase-Only Pulse Shaping and the Genetic Algorithm," Photonics **7**(3), 69 (2020).
8. A. M. Weiner, "Femtosecond pulse shaping using spatial light modulators," Rev. Sci. Instrum. **71**(5), 1929–1960 (2000).
9. PicoLAS, "PLCS-40," https://picolas.de/shop/accessories-en/plcs-40/.
10. M. Michalska, J. Swiderski, and M. Mamajek, "Arbitrary pulse shaping in Er-doped fiber amplifiers—Possibilities and limitations," Opt Laser Technol. **60**, 8–13 (2014).
11. G. Sobon, P. Kaczmarek, A. Antonczak, J. Sotor, A. Waz, and K. M. Abramski, "Pulsed dual-stage fiber MOPA source operating at 1550 nm with arbitrarily shaped output pulses," Appl. Phys. B **105**(4), 721–727 (2011).
12. P. Wan, J. Liu, L. Yang, and F. Amzajerdian, "Pulse shaping fiber lasers for free-space and lidar applications," Proc. SPIE **7817**, 78170K (2010).
13. P. Adamiec, A. Machón, M. Rodríguez-Cortina, A. L. Moya, E. Cordero, and J. Barbero, "LIDAR echo emulator," Proc. SPIE **11180**, 65 (2019).
14. M. Rodríguez-Cortina, P. Adamiec, J. Barbero, X. Quintana, and M. A. Geday, "Emulation Technique of Multiple Overlapped Return Echoes of a Spatial LIDAR With 100-dB Dynamic Resolution," IEEE Trans Instrum Meas. **70**, 1–7 (2021).
15. A. Dumas, J. Rothman, F. Gibert, D. Édouart, G. Lasfargues, C. Cénac, F. Le Mounier, J. Pellegrino, J. Zanatta, A. Bardoux, F. Tinto, and P. Flamant, "Evaluation of a HgCdTe e-APD based detector for 2 µm CO2 DIAL application," Appl. Opt. **56**(27), 7577–7585 (2017).
16. V.G. Dmitriev, G.G. Gurzadyan, and D.N. Nikogosyan, *Handbook of Nonlinear Optical Crystals*, 3rd ed., (Springer Series in Optical Sciences book series, 1999)
17. I.D. Villar and I.R Matias, *Optical Fibre Sensors: Fundamentals for Development of Optimized Devices*, (John Wiley & Sons, 2020).
18. H. Yu, Z. Pan, H. Zhang, and J. Wang, "Recent advances in self-frequency-doubling crystals," Journal of Materiomics **2**(1), 55–65 (2016).
19. M. Sabaeian M, L. Mousave, and H. Nadgaran, "Investigation of thermally-induced phase mismatching in continuous-wave second harmonic generation: A theoretical model," Opt. Express **18**(18), 18732–43 (2010).
20. S. Favre, T. Sidler, and R. Salathé, "High-power long-pulse second harmonic generation and optical damage with free-running Nd:YAG laser," IEEE J. Quantum Electron. **39**(6), 733–740 (2003).
21. W. Zhang W, H. Yu, H. Wu, and S. Halasyamani, "Phase-Matching in Nonlinear Optical Compounds: A Materials Perspective," Chem. Mater. **29**(7), 2655–2668 (2017).
22. R. K. Jamal and R. K. Rustum, "Increasing the conversion efficiency of KTP crystal using the pump-power technique," Iraqi Journal of Physics **18**, 44 (2020).
23. A. A. Lagatsky, C. T. A. Brown, W. Sibbett, S. J. Holmgren, C. Canalias, V. Pasiskevicius, F. Laurell, and E. U. Rafailov, "Efficient doubling of femtosecond pulses in aperiodically and periodically poled KTP crystals," Opt. Express **15**(3), 1155–1160 (2007).
24. W. Nie, Y. Jia, J. R. Vázquez de Aldana, and F. Chen, "Efficient Second Harmonic Generation in 3D Nonlinear Optical-Lattice-Like Cladding Waveguide Splitters by Femtosecond Laser Inscription," Sci Rep. **6**(1), 22310 (2016).
25. M. Rodríguez-Cortina MR, P. Adamiec, J. Barbero J, X. Quintana, and M. A. Geday, "Development of a NIR-VIS-UV lidar echo emulator," Proc. SPIE **11852**, 330 (2021).
26. NKT Photonics, "Large mode area photonic crystal fibers," https://www.nktphotonics.com/lasers-fibers/product/large-mode-area-photonic-crystal-fibers/.
27. Fibercore, "Pure Silica Core SM Fiber," https://fibercore.humaneticsgroup.com/products/single-mode-sm-fiber/pure-silica-core-sm-fiber/sm300-sc